UNIVERSITÀ DEGLI STUDI DI PADOVA
Dipartimento di Fisica e Astronomia *"Galileo Galilei"*

Corso di Laurea in Astronomia

Performance study of new photosensors for Gamma-Ray Astronomy

Laureanda:
Irene Salmaso

Relatore:
Prof. Mosè Mariotti
Correlatore:
Dr. Manuela Mallamaci

Anno Accademico 2017/2018

To those who make my life brighter

"Considerate la vostra semenza:
fatti non foste a viver come bruti,
ma per seguir virtute e canoscenza."
(Divina Commedia, Inferno, vv. 118-120)

Contents

Summary

I fotoni nel range energetico della luce gamma non possono essere rilevati da terra per via dell'assorbimento atmosferico. È possibile tuttavia studiare i raggi gamma attraverso gli effetti che essi producono un volta entrati a contatto con gli atomi dell'atmosfera terrestre. Il fotone, interagendo con questi ultimi, produce una coppia elettrone-positrone, che a sua volta emette fotoni di bremstrahhlung. Si innesca così una cascata di particelle secondarie che possono essere rivelate da terra. La tecnica di osservazione Cherenkov si basa sul principio di emissione della luce Cherenkov, secondo cui se una particella carica attraversa un mezzo con una velocità superiore a quella della luce nel mezzo viene emesso un lampo di luce. Lo sciame innescato dalla particella primaria viene 'fotografato', attraverso la luce Cherenkov prodotta dalle particelle cariche in esso, successivamente rilevata dalla camera posta nel piano focale del telescopio. Attraverso lo studio delle immagini raccolte si può risalire a energia e direzione della particella iniziale. Combinando le immagini prodotte da più telescopi, è possibile ottenere una completa ricostruzione tridimensionale dello sciame che permette di determinare con maggior precisione energia e direzione del fotone incidente.

Lo scopo di questa tesi è studiare e caratterizzare un nuovo tipo di sensore al silicio, detto SiPM (Silicon Photomultiplier). In particolare, il sensore oggetto di studio è un array di fotodiodi a valanga che lavorano in modalità Geiger. Il sensore viene testato in guagagno, rumore ed efficienza, al variare di voltaggio e angolo di vista, all'interno di una camera oscura tramite l'utilizzo di due laser LED a diversa lunghezza d'onda. L'analisi qui presentata può essere utilizzata per valutare i vantaggi dell'implementazione di questa nuova tecnologia nella camera dei Large Size Telescope presso il Cherenkov Telescope Array.

Il lavoro è presentato con una suddivisione in quattro capitoli, oltre all'introduzione e alle conclusioni:

- Nel primo capitolo si introducono l'astronomia gamma e alcuni concetti di base inerenti l'effetto Cherenkov e lo studio dei dati raccolti. Vengono inoltre presentati gli esperimenti attivi e futuri.
- Nel secondo capitolo si descrivono brevemente le caratteristiche generali dei SiPM, con particolare attenzione al confronto con i fototubi, di cui i SiPM sono un'evoluzione.
- Il terzo capitolo raccoglie gli elementi utili alla ricostruzione del setup sperimentale.
- Nel quarto capitolo ci si concentra sulla descrizione del metodo usato per l'analisi dei dati

raccolti durante l'esperimento. Vengono infine presentati i risultati.

Come si evincerà dall'analisi, i SiPM si sono comportati come atteso dalla teoria, presentando guadagno e cross-talk lineari con il voltaggio. Anche l'efficienza nella rilevazione dei fotoni rientra nei limiti aspettati. È stato perciò possibile stabilire il voltaggio operativo ottimale, che nel nostro caso è risultato essere 32 V. Per quanto riguarda l'angolo di vista, il sensore ha dimostrato un'efficacia di rivelazione fino a quasi 60° con la luce verde.
Infine, considerando il contributo di efficacia nella rilevazione dei fotoni, rispetto ai classici fototubi i SiPM raccolgono in media il 50% di luce in più. A parità di fotoni raccolti, quindi, è come se il telescopio dotato di SiPM avesse uno specchio di diametro efficace pari a 29 m anzichè 23 m.
In conclusione, si dimostra sensori di questo tipo sono ottimi per essere utilizzati in array di telescopi Cherenkov, mostrando caratteristiche peculiari di resistenza, linearità ed efficacia.

Introduction

Nowadays, many fields of physics require the detection and counting of single photons. Silicon photomultipliers are surely best fitted for this purpose. One of the possible applications is the detection of Cherenkov radiation. This is characterized by a relatively low number of photons and as a consequence a significant detection efficiency is fundamental.
In this work, we studied the characteristics and performances of a newly designed silicon photomultiplier – from here on referred to as SiPM –. The aim of this work is to understand the feasibility for an upgraded camera to be installed at the Large Size Telescope of the Cherenkov Telescope Array. The focus of the thesis is the characterization of the new photodetector in terms of gain, noise, efficiency to be compared with the current Photomultiplier technology to understand the merit of the possible upgrade of the camera with SiPM.

The thesis is divided in 4 chapters.

- In the first chapter the Gamma-ray Astronomy is introduced. We focus on ground-based experiments which employ the Imaging Cherenkov Atmospheric Technique and we briefly describe the future CTA experiment
- In the second chapter, the new photosensors based on SiPM technology are discussed.
- In the third chapter, the experimental setup to test the SiPM is described.
- In the fourth chapter, the measurements are presented: gain, cross-talk, noise and efficiency of the SiPM are shown as a function of voltage and incident angle of the light source.

Chapter 1

Detection of high-energy photons

The electromagnetic spectrum of light covers about 20 energy decades. In particular, wavelengths shorter than 1 pm - equivalently, in an energy range above MeV - are denoted as gamma-rays.

Stars emit mostly in optical wavelengths and thus they were historically the first cosmic sources to be studied. The energy distribution in terms of wavelength or frequency of a thermal object is generally well represented by a black-body spectrum. On the contrary, the Universe is populated by many interesting 'non-thermal' objects whose spectrum can extend up to gamma-ray energies.

Among the different sources, we can find:

- Active Galactic Nuclei
- Pulsars
- Supernova Remnants
- Micro-quasars

and many others. The study of such objects is interesting for many reasons. For example, it could provide a window to understand the origin and role of relativistic cosmic particles, how neutron stars and black holes work and the nature of the dark matter.

Terrestrial atmosphere is opaque to gamma-rays. For this reason, they can be detected by exploiting satellites. Regarding space-based experiments, it is worth mentioning the *Fermi* satellite, which has been collecting data for the last ten years, accomplishing many important discoveries. In this work, though, we are going to focus on ground-based experiments that exploit the so-called Imaging Air Cherenkov Technique (IACT).

When a gamma-ray enters in the atmosphere, it interacts with molecules and atoms producing a cascade of secondary particles known as 'shower'. This happens at a typical altitude that varies from about 10 to 20 kilometers above the ground. The first steps of the cascade are shown in Figure 1.1. The gamma-ray produces an e^--e^+ pair, each carrying about half the energy of the incoming photon. The generated particles are typically ultra-relativistic and lose energy mainly because of bremsstrahlung - emitting photons.

The emitted photons can then interact with other atmospheric atoms to produce more pairs.

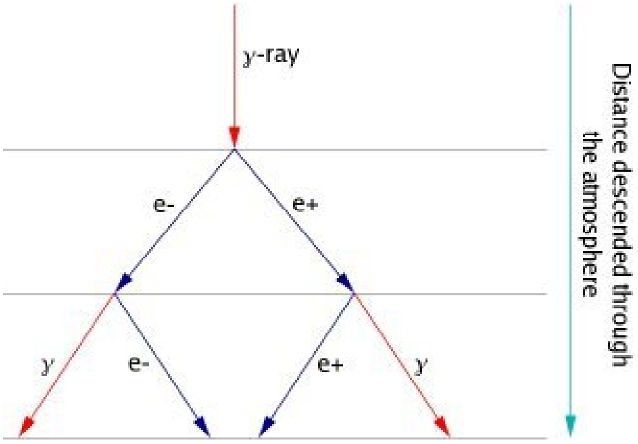

Figure 1.1: Visual representation of couple generation during a particle shower.

The process is repeated until the energy of photons and pairs is degraded, reaching the ionization limit. At this point the production of new particles is arrested because photons are no more energetic enough to generate couples and the main energy loss mechanism is ionization.

A charged particle propagating into a dielectric medium will polarize it. If it has a speed $v > \frac{c}{n}$, where c is the speed of light and n is the refraction index of the medium, it produces Cherenkov light. In fact, when the particle is relativistic, the polarization is 'late' compared to the passing time of the particle and a coherent wavefront is produced (see for example Figure 1.2). The Cherenkov light propagates in a conical wave; in the case of Cherenkov light produced in an electromagnetic shower, all the photons arrive in 2-3 ns.

On ground we cannot detect the primary gamma-ray, but it is possible to measure the secondary particles and/or the light produced by the shower in the atmosphere. In particular, this work will focus on the detection of the Cherenkov light.

Most electrons in the shower are energetic enough to emit Cherenkov light whilst passing in the atmosphere. This light is emitted with a probability that goes with $\frac{1}{\lambda^2}$, where λ is the wavelength. However, during the propagation in the atmosphere, the absorption from oxygen and ozone cuts most of the light at short wavelengths. The net result is that the typical Cherenkov spectrum is strongly peaked at 320 nm, as can be seen in Figure 1.3.

The emitted light is arranged in a typical Cherenkov cone with an emission angle of about 1°. The Cherenkov light is collected by a reflective surface and sent onto a camera placed in the focal plane of the telescope. The typical image is an ellipse, where the width is due to the geometrical lateral dimension of the shower and the length is due to elongation of the shower. If the photon that started the shower has an arrival direction aligned with the optical axis of the telescope, the ellipse will point toward the center of the camera because of a geometric effect; moreover, the distribution of intensity per pixel gives that the ellipse is more luminous in its center, that corresponds to the shower maximum development. By analyzing the parameters of this ellipse – meaning orientation, width, length, luminosity intensity distribution – we can derive direction

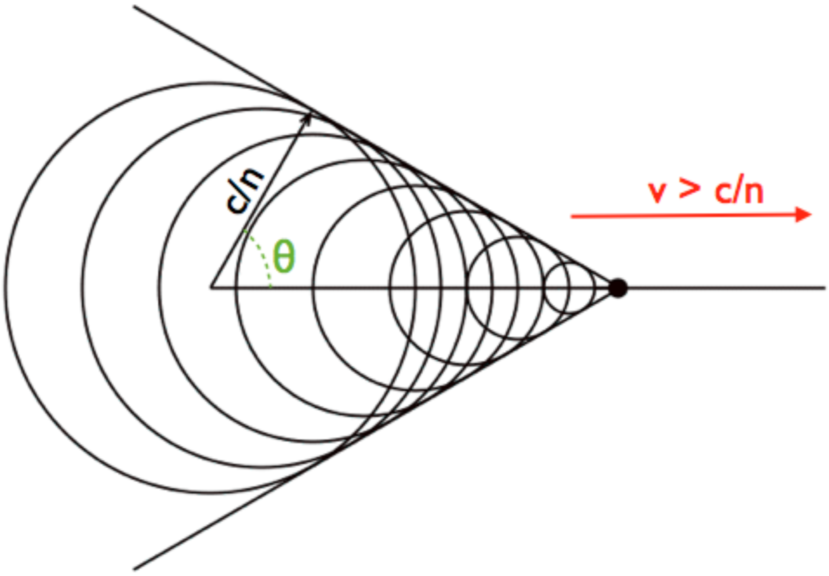

Figure 1.2: Visual representation of the wavefront generated by a relativistic particle in a dielectric medium.

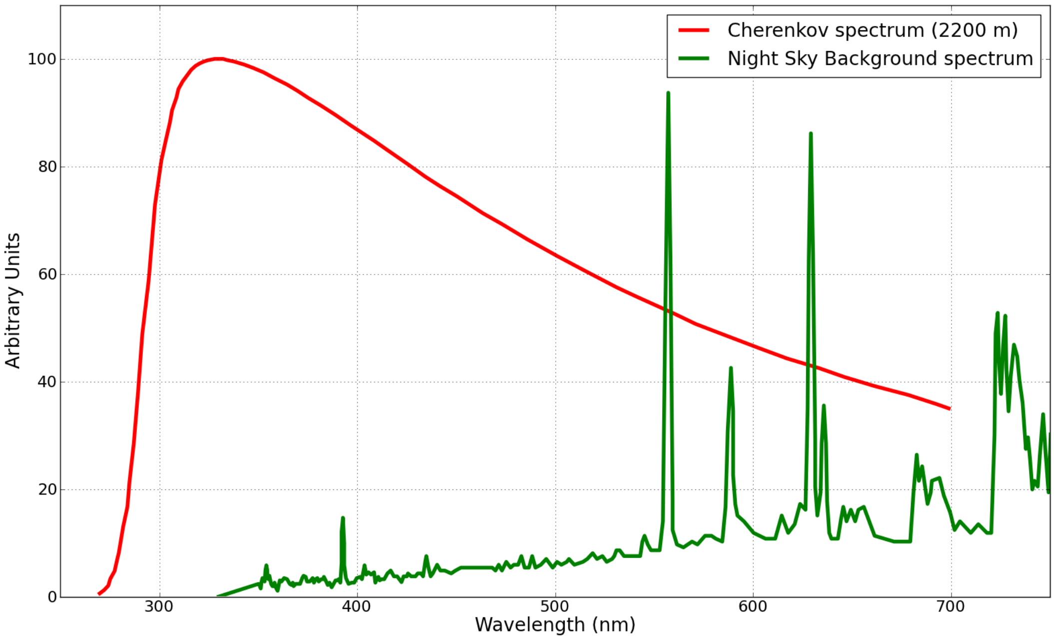

Figure 1.3: Plot of a typical Cherenkov spectrum (in red) with respect to the night sky background (in green).

and energy of the initial photon. With two telescopes, precision can be increased: for the same event, two images will be generated that can be intersected to better infer the original direction, resulting also in a more precise evaluation of the energy. Moreover, with two telescopes, it is possible a 3D reconstruction of the shower: a good detection of the shower maximum altitude is crucial for gamma/hadron separation, giving a strong background reduction. In Figure 1.4, a schematic view of the Cherenkov shower accompanied by the resulting ellipse is shown.
The rate of gamma-ray from sources can vary from several per minute for strong sources (e. g. Crab Nebula) to few per hour for faint sources. When the Cherenkov flash from the shower hits the camera, it triggers the data acquisition, thanks to fast logic electronic coincidence. Cameras can be triggered also by cosmic rays - usually, protons - that interact with atmospheric particles. The process of hadronic shower is similar to the electromagnetic shower one, but it results in different, more irregular patterns that can be therefore separated from those due to the gamma-ray that initiated the shower, more homogeneous and orientated toward a specific direction.

Given the short duration of the Cherenkov effect, and also the need to have a good signal-to-noise ratio ($\frac{S}{N}$), light capture and integration must not exceed 2-3 ns, meaning that the sensors must be fast. CCDs are thus not suited for the task, as they need longer integration. Moreover, since the signal is faint, large collection areas are necessary. Parabolic mirrors are often employed, having the advantage of being isochronous, thus maintaining the signal compact in time.
MAGIC, H.E.S.S. and VERITAS are array of Cherenkov telescopes that, at the present time, are operating through IACT. These experiments have all obtained great successes in the detection of gamma-rays, but new, more ambitious projects as CTA are currently in development.
CTA (Cherenkov Telescope Array) is a big project that aims to deploy more than one hundred

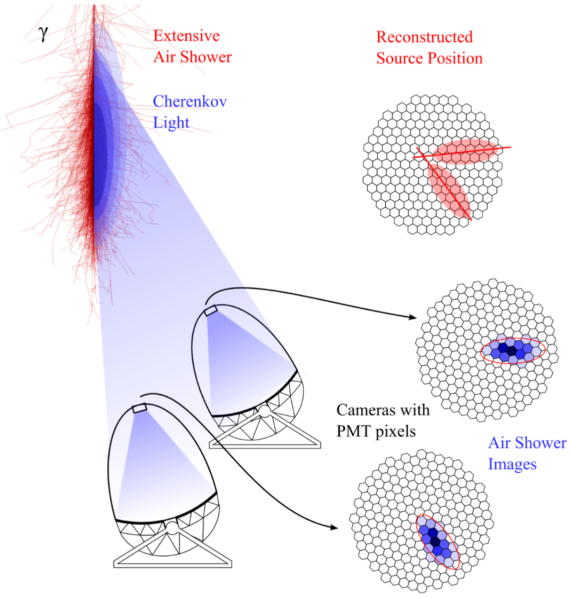

Figure 1.4: Schematic view of a Cherenkov shower. The ellipse results from the projection of the cone on the ground.

Cherenkov telescopes all around the globe to detect and cross-check particle showers. There will be three classes of telescope of different size, that in their totality will be sensitive to energies from 20 GeV up to 300 TeV. Figure 1.5 is a picture of the future CTA array: the three different sizes of telescopes are clearly visible. In particular, the main scientific targets of CTA will be:

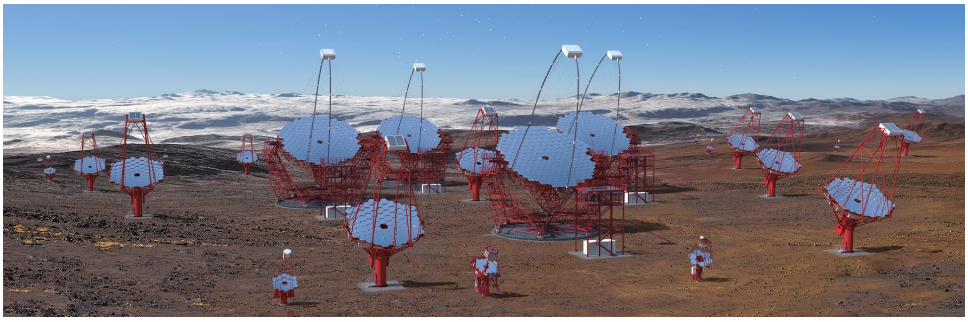

Figure 1.5: Picture of the Cherenkov Telescope Array.

- The Galactic Centre, with its richness in gamma-emitting sources such as supernova remnants, molecular clouds and pulsars, and also the supermassive central black hole.
- The Large Magellanic Cloud (LMC), because of its relative proximity to our galaxy and the large number of supernova remnants and H II regions.
- The Galactic Plane, to hopefully discover new phenomena and highly energetic sources in the galaxy.
- Galaxy Clusters, that are expected to contain many accelerated cosmic rays and are mainly composed of dark matter.
- Active Galactic Nuclei, to understand the physics and phenomenology related to them, but also the mechanisms related to cosmic-ray production and gamma-ray cosmology.
- Transient phenomena, because their short-timed, intense, energetic activity is associated with extreme objects such as neutron stars and black holes.

Efficient and fast sensors are necessary for the success of CTA experiment: the speed of the camera is crucial in the detection of the showers, whilst efficiency in photodetection means that a telescope virtually gains size, being able to detect more photons and all the while keeping construction costs lower.

This thesis will focus on the characterization of a sensor based on silicon photomultipliers technology. This kind of sensor would be optimal to be used in the CTA Large-Sized Telescopes (LST) camera, although the technology is suitable not only for other telescopes, but also different kinds of scientific instrumentation, as neutrino and dark matter detectors.

It is worth mentioning that SiPM technology is already successfully exploited for the First G-APD Cherenkov Telescope (FACT) and for the Small-Sized Telescopes of CTA.

Chapter 2

Silicon Photomultipliers

In order to measure fast light pulses, photomultipliers are usually employed.
Photomultipliers are devices that, when hit by a photon on the photocathode, generate a certain number of electrons - the exact number depending on the gain of the multiplication chain. Photoelectrons will undergo towards a series of dynodes creating an electric pulse, with an overall gain in charge that depends on the voltage applied.

Photomultipliers (see Figure 2.1) are the most common type of phototube. In general, they have an entry window for photons in which a photocatode material is deposited, usually an alkali material. When a photon impacts on its surface, an electron can be emitted via photoelectric effect with a probability called Quantum Efficiency (QE). An electric field then accelerates the

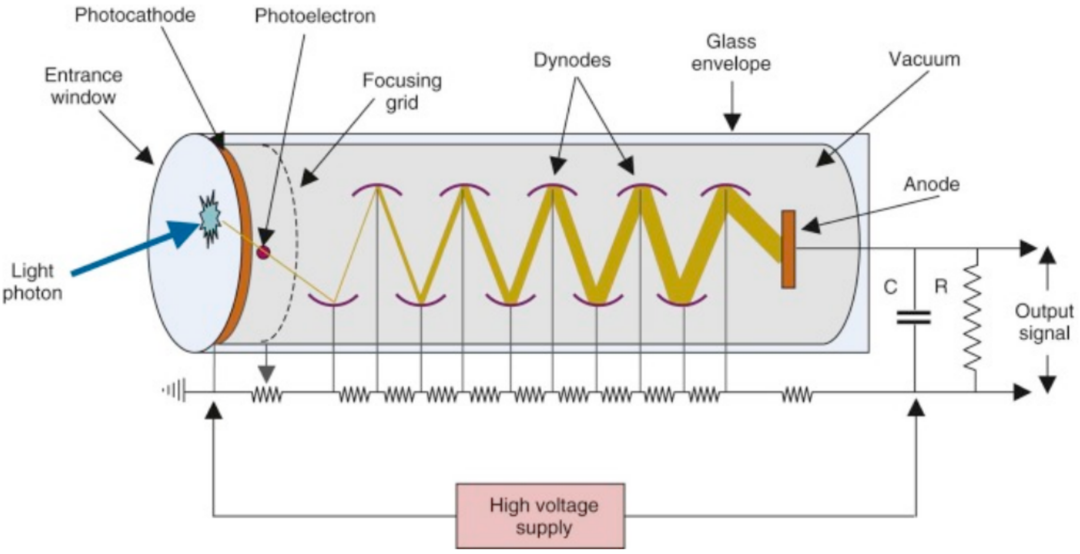

Figure 2.1: Schematic representation of a photomultiplier.

photoelectrons on the first dynode. During the impact, about 4 or 5 electrons are extracted per each photoelectron, which in turn are accelerated by the electric field and hit another dynode. This process is repeated several times until the anode is reached. This amplification is necessary, since a final charge of several electrons (typically 10^5) is needed to detect and resolve the single incident photon from electronic noise. Once the final charge is detected and recorded, we can deduce information on the incoming photon flux.
Classical photomultipliers have a series of advantages, which are:

- The small cost of a fairly big photocathode
- The fact that the noise does not increase much with photocatode dimension

On the other hand, there are also some disadvantages. Among them, we recall:

- The fragility of the structure, also subjected to aging
- The need for high voltage to operate
- The limited QE
- The sensitivity to Earth magnetic field

In order to overcome some of these issues, a novel technology of photon detection based on solid state devices is nowadays available, called Silicon Photomultiplier (SiPM).
A SiPM consists of an array of several Geiger Mode Avalanche Photodiodes that discharge when hit by a photon (Figure 2.2 provides a close view to a SiPM).
Photodiodes are formed by a particular junction, called p-n junction, built combining two semiconductors of opposite doping (see Figure 2.3). The entire photodiode is neutral on average, while in the middle the junction causes a depletion region, meaning that there is a potential difference that generates an electromagnetic field.

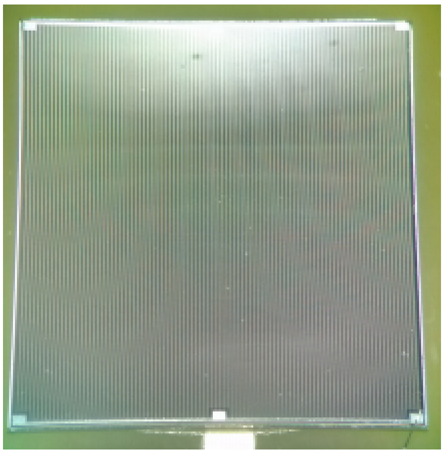

Figure 2.2: View of one of the SiPMs employed in this work, 6×6 mm^2, as seen with the aid of a microscope. The small dotted texture seen in the picture are in fact the single Geiger mode avalanche photodiodes array that the SiPM is made of.

A photodiode directly polarized behaves in the exact same way as a normal diode, but if it is inversely polarized the depletion region grows and the electromagnetic field increases consequently. When an energetic photon hits the sensor, it can create an electron-hole pair because a valence electron is brought in the conduction band. The pair is then accelerated by the electric field and moves towards the electrodes. The resulting electric current is proportional to the number of incident photons. The moving electron can then generate other electron-hole pairs and the avalanche that results can reach a value 1000 times higher than the initial charge. In principle, also holes can cause an avalanche, but their threshold is higher than for electrons. Such an energy is reached at a voltage called Breakdown Voltage, $V_{breakdown}$, after which the avalanche breaks down and the device enters the so-called Geiger mode. In this mode, the incident photon will cause the first generated electron-hole pair to trigger the avalanche. Once the current is flowing, it is quenched through a series of resistors, so that the reverse voltage that the diode is undergoing becomes lower than $V_{breakdown}$ and thus the diode can recharge back to its bias voltage and it is ready to detect other photons. The signal is no more proportional to the number of incident photons, because the charge signal is charge accumulated in the inverse polarized diode seen as as a capacitor, so it is independent of the number of photons that triggers the avalanche. An array of many Geiger mode Avalanche Photodiodes is the basic concept of a SiPM. The devices that function in Geiger mode are then specialized to detect single photons, so they are particularly apt to be used in the Cherenkov technique, where photons are few and far in between. Every incident photon might start an avalanche in a cell, but SiPMs are arrays of many cells, so that the probability of two or more photons hitting the same cell at the exact same time is negligible.

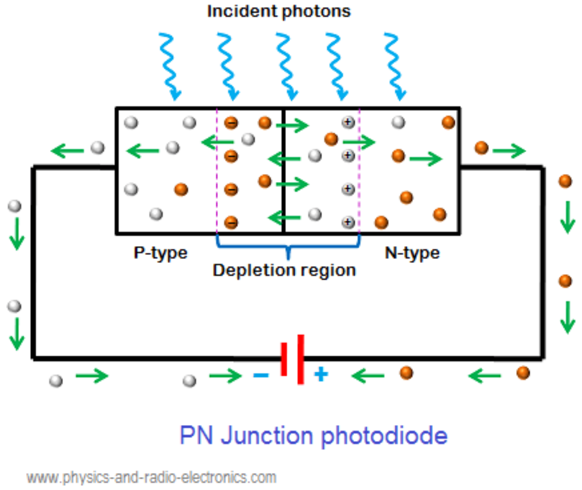

Figure 2.3: Schematic representation of a photodiode.

In order to characterize a SiPM, four parameters are usually employed:

- Gain
- Noise

- Cross-talk
- Photodetection efficiency (PDE)

The gain is the quantity of charge generated by a single incident photon or electron. It is an amplification that originates in the device; in other words, it is the charge of an avalanche. The gain and its variation with voltage - and temperature - should be properly measured to correctly characterize also the other parameters.

The noise is a typical feature of electronic devices and is represented by the width of the signal that, instead of being perfectly centered on a single value, is spread across a more or less wide interval of values, depending on the uncertainty of the measurements. It includes the features of the electronic amplification and of the readout. Another important source of noise is the dark count rate (DCR): thermal electrons can be generated inside the device and then 'promoted' from the valence band in the conduction band by thermal energy and they are able to initiate an avalanche even without an external signal. With increasing temperature, the noise increases and thus it is important to maintain a constant temperature, possibly low, for the duration of the measurement.

Cross-talk is another source of additional noise. When the avalanche is triggered by an incident photon, electrons developed in the avalanche can emit an infrared photon that can start a secondary avalanche in neighboring micro-cells. In the final signal, then, we have a total number of avalanches that is higher than the original avalanches number caused by incident photons.

PDE (photon detection efficiency) is the probability for a photon that impact on the detector to produce an avalanche. It is a function of temperature, voltage and wavelength, among others. In particular, we note that for SiPMs PDE is given by:

$$PDE_{SiPM} = P_{transmission} \times QE \times P_{avalanche} \times \epsilon_{fillfactor} \tag{2.1}$$

where $P_{transmission}$ is the probability that a photon enters the depletion region, QE is the quantum efficiency, the probability of creating an electron-hole pair, $P_{avalanche}$ is the probability that the electron-hole pair initiates an avalanche and $\epsilon_{fillfactor}$ quantifies the ratio of active area with respect to the total area.

The advantages of SiPMs are:

- Robustness, as they can resist physical and light strain
- Low voltage needed
- High PDE
- Next to none sensitivity to magnetic fields
- Low costs of construction

It is expected that SiPMs can reach very high PDE. Figure 2.4 compares PDE fot different sensors. Figure 2.4 (a) shows the QE for different types of PMT of the version that will be used for LST. Figure 2.4 (b) reports the PDE in particular for the SiPMs adopted in this work (FBK HD3_2 6 × 6 mm^2). Table 2.1 provides a comparison of detection efficiency for SiPMs and classical photomultipliers at different wavelengths. It is evident that SiPMs efficiency in detecting photons is very high - almost 60% - for UV wavelengths and it is always higher than for PMs.

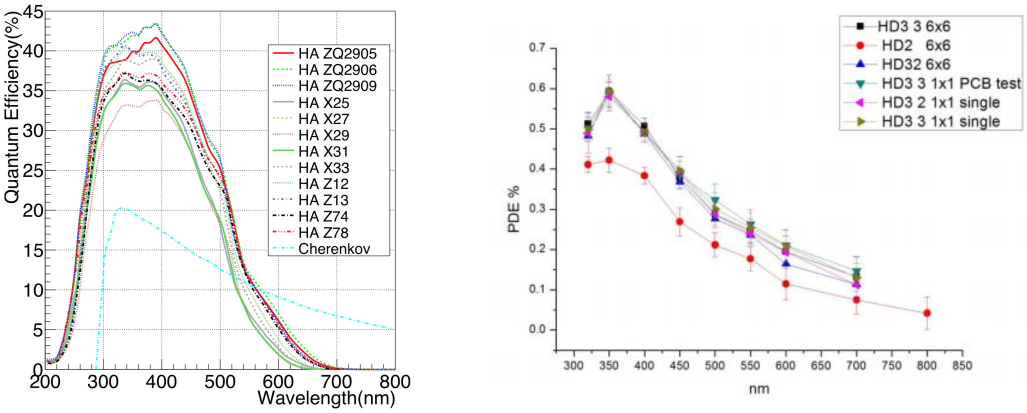

(a)

(b)

Figure 2.4: (a) PDE of LST phototubes. (b) PDE derived for different SiPMs, we used HD3_2. Private communication with Dc. L. Consiglio, INFN Naples.
Notice that SiPMs show a photon detection efficiency almost twice the PDE derived for phototubes.

λ	PDE_{SiPM}	QE_{PM}
350	0.6	0.42
400	0.5	0.42
450	0.4	0.3
500	0.3	0.2
550	0.25	0.1
600	0.2	0.05
650	0.18	0.03
700	0.15	0
750	0.1	0
800	0.1	0

Table 2.1: Detection efficiency for SiPMs tested in this thesis and LST photomultipliers actually used for LST camera production, at different wavelengths

Finally, it is worth mentioning that SiPMs can be clustered together to create differently shaped arrays. An example is the pixel array of 14 sensors shown in Figures 3.1 and 3.2. As the gain is supposed to behave linearly, the array should work as a sum of 14 sensors.

Chapter 3

Experimental Setup

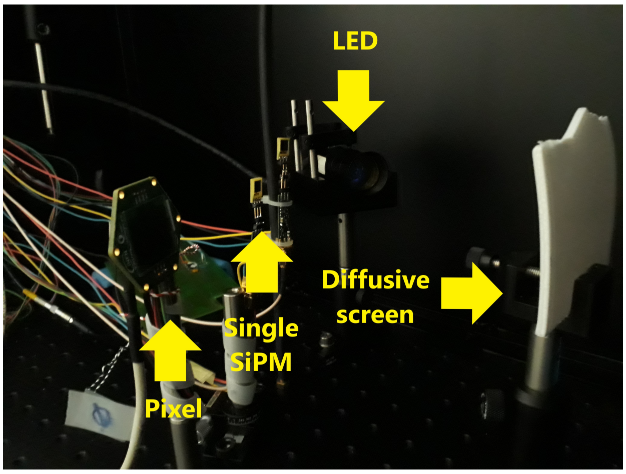

Figure 3.1: Setup of the dark room during the experiment.

The experimental setup used in this work is shown in Figure 3.1 ad consists of several elements enclosed in a light tight closed Dark Box. The main ones are:

- The light source: Lasers Picoquant: PLS 8-2-592 ($\lambda = 376nm$) and PLS 8-2-519 ($\lambda = 499nm$).
- The first type of sensor: SiPMs $6 \times 6\ mm^2$ FBK (Fondazione Bruno Kessler) near-UV version HD3_2.
- The second type of sensor: Pixel - array of 14 identical SiPMs version HD3_2. Figure 3.2 provides a better view of the matrix.

The box temperature was also monitored and recorded thanks to several thermal probes inside the dark box. The signal from the SiPM is amplified by a dedicated amplifier powered by a symmetric voltage of -3.3 V and 3.3 V connected to each sensor. For data acquisition a DRS4

(Data Ring Sampler 4) or an oscilloscope Tektronix DP07354 were used.

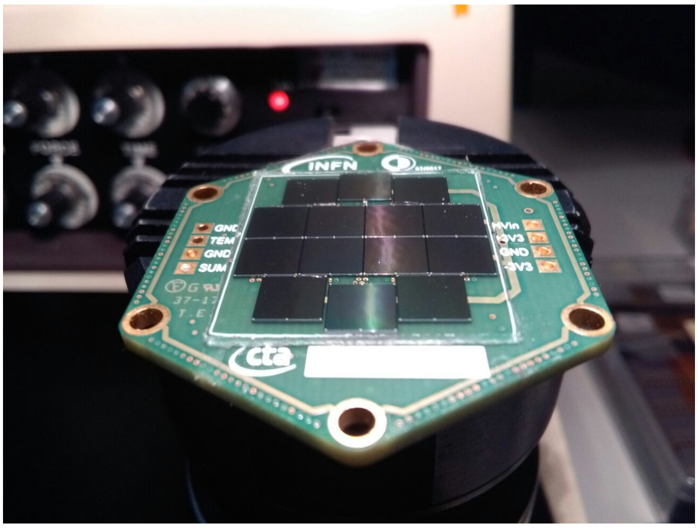

Figure 3.2: Picture of the 14-sensors pixel used in the experiment.

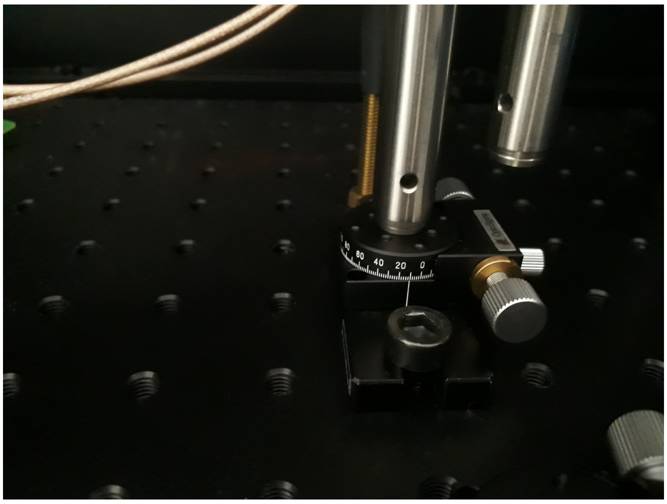

Figure 3.3: Picture of the goniometer.

The laser is pointed towards a diffusive screen whose function is to spread the incident light in an homogeneous beam of almost spherical waves. In the first part of the experiment, only single SiPMs were used, while in the second part also the 14-sensors pixel was employed.
In the latter part of the experiment, a diaphragm was added to the screen in order to obtain a smaller and geometrically better defined source, whereas the single SiPM and the pixel were mounted on a goniometer (Figure 3.3).
The distance between the diffusive screen and the SiPMs is 27 cm, while there are 10.5 cm from

the diffusive screen to the head of the laser. The total width of the laser light spot on the screen is 7 cm, reduced to 1 cm when diaphragmed.

Chapter 4

Experimental procedure and Data Analysis

The aim of this work is to make a full characterization of the sensor and find its optimal working point. We have therefore evaluated the parameters of gain, efficiency, cross-talk, signal-to-noise ratio as a function of operating voltage and incident angle. The number of photons detected by a single photosensor is expected to follow the Poissonian distribution

$$P(n,\mu) = \frac{\mu^n}{n!}e^{-\mu} \tag{4.1}$$

The Poissonian distribution has average and standard deviation that are μ and $\sqrt{\mu}$, respectively. μ is the average number of photons that are detected - in the sense that they generated an avalanche - while n is the number of photons detected in a given event. The number of detected photons does not follow the Poissonian statisctics because of the cross-talk probability. Only the probability of detecting zero photons does not depend on the cross-talk:

$$P(0,\mu) = e^{-\mu} \tag{4.2}$$

On the other hand, the theoretical probability of detecting one photon will be

$$P(1,\mu) = \mu e^{-\mu} \tag{4.3}$$

However, the latter is affected by the cross-talk, that reduces the probability to measure the single event by the cross-talk probability, thus we shall modify it to

$$P(1,\mu)^* = \mu e^{-\mu}(1 - P_{ct}) \tag{4.4}$$

where P_{ct} is the cross-talk probability. $P(0,\mu)$ and $P(1,\mu)^*$ can be measured experimentally. In order to do so, a series of signals at fixed conditions were taken and the actual peak height (in mV) was derived. An example of peak height distribution can be seen in Figure 4.1. The distribution is similar to a sum of Gaussian functions. Each distinct peak represents the events

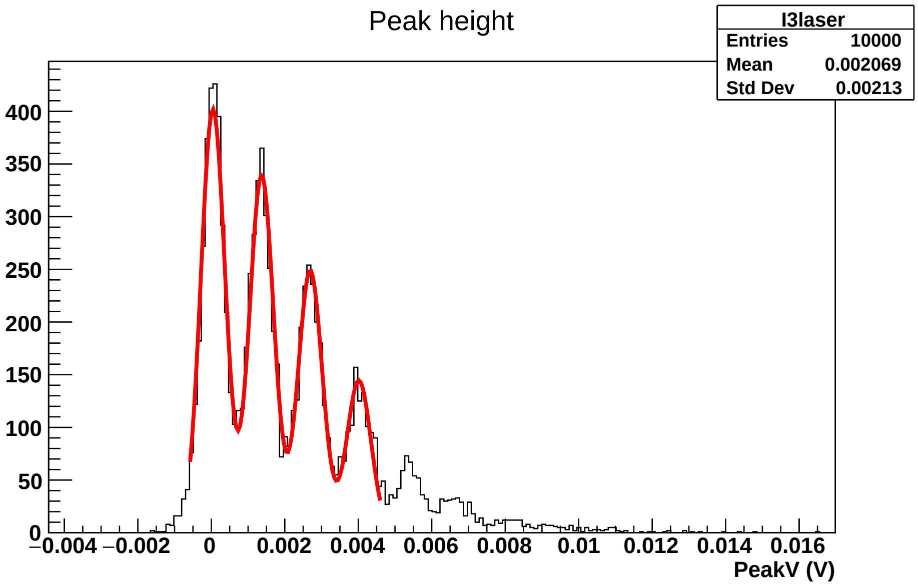

Figure 4.1: Example of a distribution of peak height of the signal obtained at 34 V for UV wavelength. The red curve is the fit discussed in the text.

corresponding to the detection of zero, one, two or three photons.
To characterize the SiPM, we used the gain, the cross-talk probability, μ and μ^*. The latter is a quantity related to S/N, where S is the average signal and N is the standard deviation, as

$$\mu^* = \left(\frac{S}{N}\right)^2$$

The width of the Gaussian function represents the overall noise (electronic and dark count tails) in that particular dataset. The distance from two consecutive peaks represents instead the gain of the detector, expressed in mV/detected photon.
In an ideal situation, the gain is linear and the cross-talk probability is low, so that it is easy to estimate the effective number of incoming photons. Moreover, μ and μ^* should be the same.
In order to extract these parameters, we fit the data by means of a Python script in which the following function is implemented:

$$f(V) = A_0 \exp\left(-\frac{(V-V_0)^2}{2\sigma_0^2}\right) + A_1 \exp\left(-\frac{(V-V_1)^2}{2\sigma_1^2}\right) + A_2 \exp\left(-\frac{(V-V_2)^2}{2\sigma_2^2}\right) + A_3 \exp\left(-\frac{(V-V_3)^2}{2\sigma_3^2}\right) \tag{4.5}$$

which is basically a sum of four Gaussian functions with eight free parameters, where

$$V_1 = V_0 + g$$

$$V_2 = V_0 + 2g$$

$$V_3 = V_0 + 3g$$

$$\sigma_1^2 = \sigma_0^2 + \sigma_{add}^2$$
$$\sigma_2^2 = \sigma_0^2 + 4\sigma_{add}^2$$
$$\sigma_3^2 = \sigma_0^2 + 9\sigma_{add}^2$$

A_0, A_1, A_2, A_3 are the amplitude of the gaussians, V_0 is the average value of the first gaussian, g is the gain and corresponds to the difference between the average values of the first and second gaussians, σ_0 is the width of the first gaussian and σ_{add} is the additional noise that adds to σ_0. The gain is simply $V_1 - V_0$. $P(0, \mu)$ and $P(1, \mu)^*$ are derived from the area of the first Gaussian. It is possible then to derive μ through equation 4.2 and then $P(1, \mu)$ from equation 4.3. Thus P_{ct} can be calculated as follows:

$$P_{ct} = 1 - \frac{P(1, \mu)^*}{P(1, \mu)} \tag{4.6}$$

The data-taking was performed as follows: the LED laser beam is directed and diffused by a white screen (see Figure 3.1). The laser intensity can be adjusted for specific measurements. Two sensors are necessary, since the LED could spontaneously change the intensity during the time of data-taking. One SiPM then is used as a reference to normalize the signal. For the green light, the voltage was changed from 29 V to 36 V in steps of 1 V. 20000 waveforms were recorded for each voltage. For the UV light, 10000 waveforms were found to be sufficient. The voltage was varied from 31 V to 36 V since at 29 V and 30 V the fit was found to give too large errors in that particular dataset. For each waveform, the peak height of the signal has been extracted and a distribution has been built as shown in Figure **??**.

By applying the fit we derived the results for both wavelengths shown in Tables 4.1 and 4.2 and Figures from 4.5 to 4.3. Statistical uncertainties were inferred through the error propagation of statistical errors on fit parameters.

Voltage (V)	gain (mV)	μ	P_{ct}%	μ^*
31	1.165±0.007	0.990±0.025	12.42±2.33	0.85
32	1.422±0.006	1.100±0.024	14.17±2.10	0.88
33	1.704±0.006	1.139±0.023	20.95±1.98	0.87
34	1.955±0.007	1.174±0.027	24.58±2.05	0.86
35	2.239±0.008	1.190±0.028	27.80±2.03	0.82
36	2.505±0.009	1.209±0.029	32.71±1.91	0.79

Table 4.1: Results of the analysis of data obtained with UV light.

As expected, the gain is found to increase linearly with respect to the voltage. Also P_{ct} is found to increase with the voltage. The laser intensity was kept constant and normalized, so that both cross-talk and PDE are proportional to μ, as it is shown in Figure 4.4. Since P_{ct} and PDE are increasing with the bias voltage, the optimal working condition has to be selected by looking to the ratio S/N. In Figure 4.5 μ^* is shown as a function of bias voltage for UV and green light. One can see that for the UV light 32 V is the best working condition: for lower voltages the efficiency is too low, whereas for higher voltages the cross-talk introduces more noise. In the case of green light, there is no a real 'optimum' voltage: at 32 V a plateau is reached, which means

Voltage (V)	gain (mV)	μ	$P_{ct}\%$	μ^*
29	0.930±0.006	1.416±0.029	13.75±2.66	1.55
30	1.186±0.004	1.783±0.028	10.16±2.36	1.70
31	1.468±0.004	1.921±0.027	17.97±2.15	1.70
32	1.762±0.004	2.068±0.027	18.04±2.12	1.75
33	2.043±0.005	2.184±0.029	18.42±2.29	1.75
34	2.337±0.006	2.270±0.030	24.72±2.27	1.75
35	2.607±0.007	2.354±0.031	29.10±2.28	1.77
36	2.886±0.008	2.393±0.042	30.63±2.32	1.74

Table 4.2: Results of the analysis of data obtained with green light.

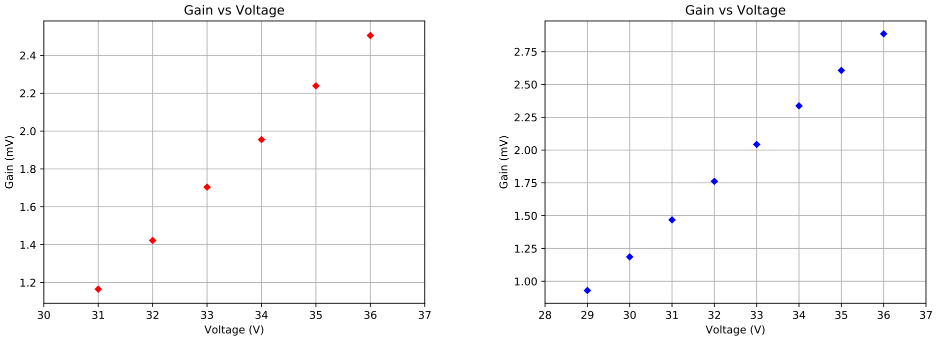

(a)

(b)

Figure 4.2: Plot of the gain with respect to the voltage using UV light (a) and green light (b).

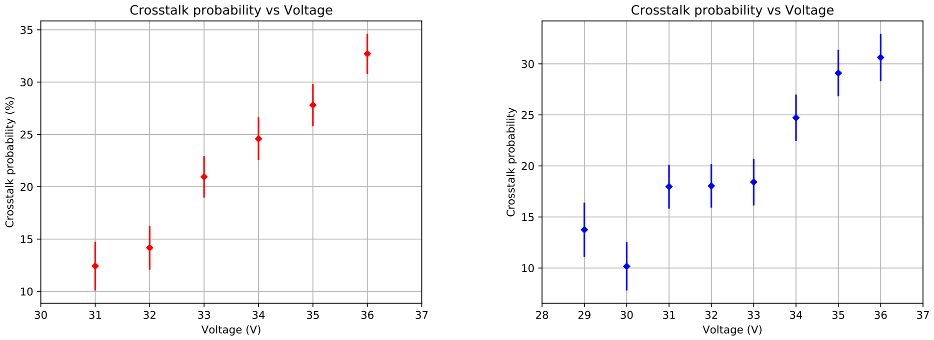

(a)

(b)

Figure 4.3: Plot of P_{ct} with respect to the voltage using UV light (a) and green light (b).

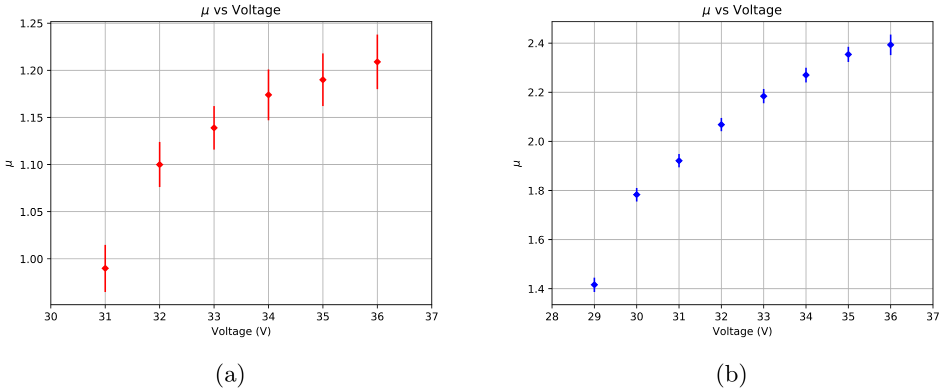

(a)

(b)

Figure 4.4: Plot of μ with respect to the voltage using UV light (a) and green light (b).

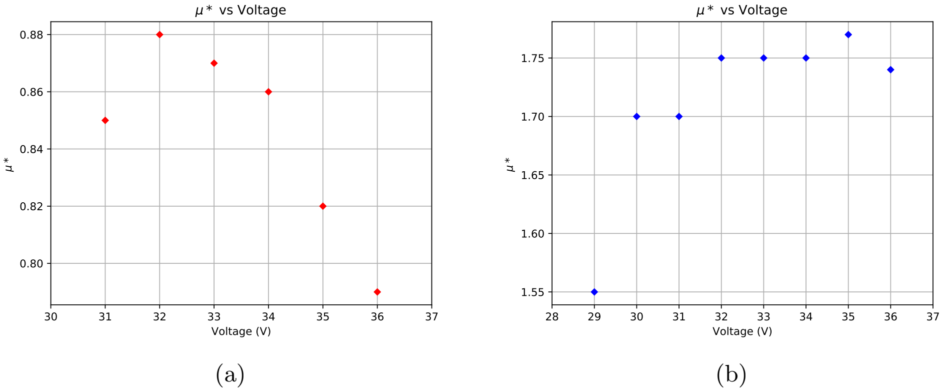

(a)

(b)

Figure 4.5: Plot of μ^* with respect to the voltage using UV light (a) and green light (b).

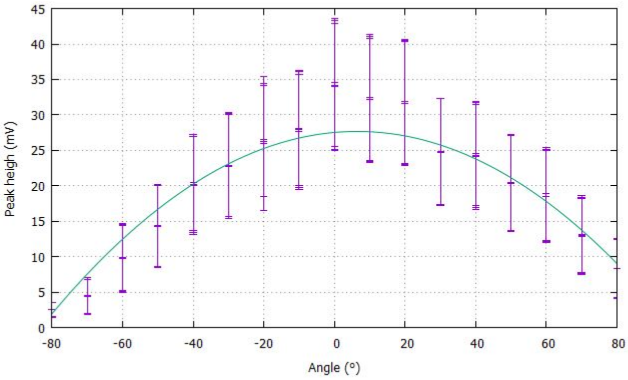

Figure 4.6: Average peak height of the signal as a function of the angle. In this case the real zero was found to be at 5°.

that higher cross-talk is compensated by higher efficiency. 32 V is then the optimal working voltage for the studied sensors for UV, but it is good also for the green.
As described in chapter 3, the second part of the measurements are aimed to analyze the performances of the SiPM efficiency as a function of the incident angle, deriving the response curve of the signal distribution.
The setup was slightly different: two identical SiPMs were put in the dark room, one facing the diffusive screen as before whilst the other was equipped with a rotating mechanism that allowed it to move on its axis (a closer picture of the goniometer mounted on said mechanism is shown in Figure 3.3).
We measured the average peak height of 3000 waveforms for each angle, from $-90°$ to $90°$ in steps of $10°$. The measurement was repeated three times for each angle, then average values and statistical errors were calculated. The procedure was repeated using both LEDs.
In order to determine the variation of the photon detection as a function of the angle, one should also remember that at large angles the area exposed to the beam of light is smaller than when the sensors are face-on. A correction in terms of the effective area is then needed, since the latter decreases with increasing angles. This correction can easily be realized by dividing the results by $cos(\theta)$, measured from the normal where $0°$ means that the sensor is face-on and the signal is maximum. At $90°$, instead, no signal is expected. This is not generally true. Although small, there is a residual signal at $90°$, due to electronic noise and some scattered photons. It was then chosen to directly subtract this noise from our data. Furthermore, in order to minimize fluctuations due to diffused scattered photons inside the dark room, we decided to evaluate an average value for each symmetric dataset ($-\theta$, θ).
We set the starting position corresponding to $0°$ by fitting the data with a parabolic function ($y = ax^2 + bx + c$) and the vertex – which corresponds to the real zero – was derived analytically with the well-known formula $V_x = -\frac{b}{2a}$. Data were thus rescaled when needed.
An example of the parabolic fit on the data can be seen in Figure 4.6.
Results, already rescaled and normalized, are shown in Tables 4.3 and 4.4 and Figure 4.7.

$\theta(deg)$	$\frac{mean}{cos(\theta)}$
90.0 ± 0.5	0.00 ± 0.02
80.0 ± 0.5	6.89 ± 0.03
70.0 ± 0.5	10.18 ± 0.06
60.0 ± 0.5	14.23 ± 0.09
50.0 ± 0.5	14.73 ± 0.12
40.0 ± 0.5	16.17 ± 0.14
30.0 ± 0.5	15.58 ± 0.16
20.0 ± 0.5	16.52 ± 0.18
10.0 ± 0.5	16.76 ± 0.19
0.0 ± 0.5	17.19 ± 0.19

Table 4.3: Results of the analysis of data obtained with UV light and the single SiPM.

$\theta(deg)$	$\frac{mean}{cos(\theta)}$
90.0 ± 0.5	0.000 ± 0,008
80.0 ± 0.5	19.085 ± 0.021
70.0 ± 0.5	36.876 ± 0.058
60.0 ± 0.5	41.271 ± 0.090
50.0 ± 0.5	44.929 ± 0.145
40.0 ± 0.5	45.463 ± 0.187
30.0 ± 0.5	45.560 ± 0.125
20.0 ± 0.5	45.593 ± 0.190
10.0 ± 0.5	46.242 ± 0.182
0.0 ± 0.5	47.519 ± 0.172

Table 4.4: Results of the analysis of data obtained with green light and the single SiPM.

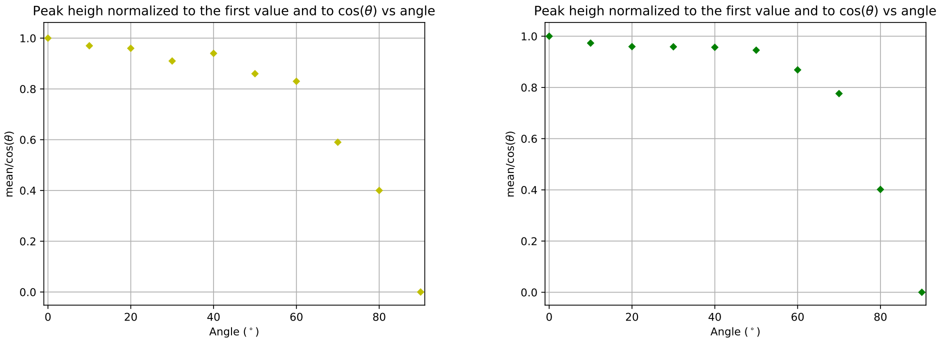

(a) (b)

Figure 4.7: Plot of the peak height with respect to the angle using UV light (a) and green light (b).

By looking at the plots in Figure 4.7, it is evident that there are some unexpected deviations from a smooth curve, similar to a modulation, that exceed the error bars, so a small but significant effect is present. In Figure 4.8 it is shown a similar curve obtained by another research group as a reference for the reader. The results we obtained are similar to those shown in Figure 4.7 for different SiPMs (Hamamatsu model).

The observed modulation could depend on a particular position of the SiPM at a certain angle that included in the detection some 'hidden' scattered photons that would otherwise been missed. The fact that the unexpected peaks take place at different angles for different wavelengths, though, seems to disrupt this hypothesis. Another possible explanation is that the optical path the photons travel in the SiPM protective coating at those angles resonates with the specific wavelength of the light. The result would be similar to an anti-reflecting glass.
The same procedure of evaluation of the response curve was repeated by using the pixel. Results are shown in Tables 4.5 and 4.6 and Figure 4.9.

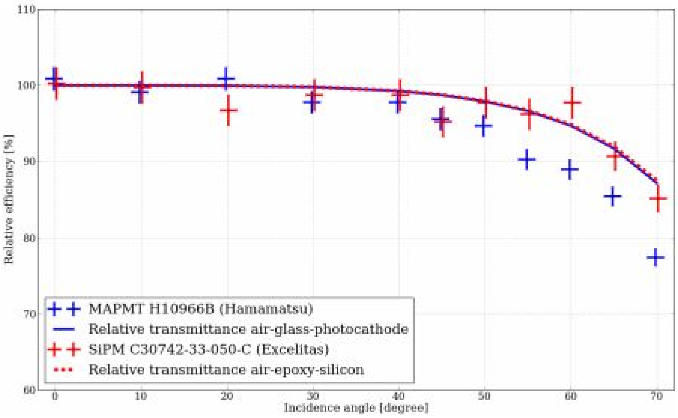

Figure 4.8: Angular efficiency of different photodetectors at 420 nm.

$\theta(deg)$	$\frac{mean}{cos(\theta)}$
90.0 ± 0.5	0.00 ± 0.15
80.0 ± 0.5	11.94 ± 0.17
70.0 ± 0.5	22.51 ± 0.23
60.0 ± 0.5	31.92 ± 0.31
50.0 ± 0.5	38.89 ± 0.40
40.0 ± 0.5	42.89 ± 0.48
30.0 ± 0.5	45.51 ± 0.54
20.0 ± 0.5	47.16 ± 0.59
10.0 ± 0.5	48.55 ± 0.63
0.0 ± 0.5	48.59 ± 0.64

Table 4.5: Results of the analysis of data obtained with UV light and the pixel.

$\theta(deg)$	$\frac{mean}{cos(\theta)}$
90.0 ± 0.5	0.000 ± 0.254
80.0 ± 0.5	171.554 ± 0.462
70.0 ± 0.5	287.267 ± 0.941
60.0 ± 0.5	329.485 ± 1.407
50.0 ± 0.5	343.449 ± 1.799
40.0 ± 0.5	345.217 ± 2.105
30.0 ± 0.5	344.886 ± 2.344
20.0 ± 0.5	346.327 ± 2.532
10.0 ± 0.5	345.256 ± 2.634
0.0 ± 0.5	344.870 ± 2.668

Table 4.6: Results of the analysis of data obtained with green light and the pixel.

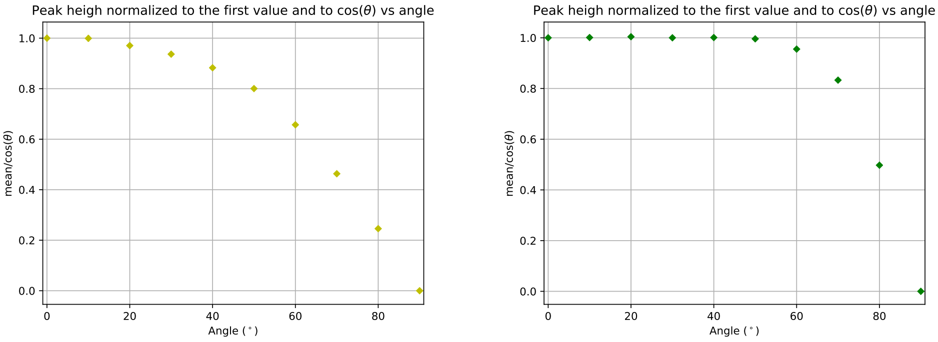

(a)

(b)

Figure 4.9: Plot of the peak height with respect to the angle using UV light (a) and green light (b).

By looking at Figure 4.9, one can see the results are more stable than those obtained with the single SiPM. This can be due to the particular coating on the pixel, added to better ensure the protection of the cluster of SiPMs. In fact, the pixel was provided with a protective resin, which probably is not very transparent in UV. This can also explain why the UV curve starts to decrease at 20° already. With green light, the curve is almost constant until the angle reaches 60°, meaning the resin is transparent to that wavelength. Since with both LEDs the modulation shown in Figure 4.7 disappears, we can state that those fluctuations were probably due to light interference with the SiPM protective coating and not by aresidual background due to multiple reflection in the dark box.

Final Remarks

In this thesis work, we studied the response of a new SiPM in terms of gain, cross-talk probability and efficiency as a function of voltage and incident angle for two wavelengths (UV and green). Regarding the first part of the experiment, the single SiPM gave a linear response in terms of gain and cross-talk with respect to the increasing voltage. Also, the distributions of μ and μ^* behaved as expected at both wavelengths. This means that SiPMs are very stable and their behavior is highly predictable, confirming their aptness as fast light pulses detectors.

In the second part of the experiment, the angular response was investigated. The modulations showed in the single SiPM response pattern discussed in chapter 4 were unexpected. It was proposed that they are due to particular resonances with the protective coating. It would be interesting to repeat the experiment with SiPMs of different manufacturers to see if the same pattern shows up. Since the pixel, which has a thick resin coating on top, showed a more regular pattern, the hypothesis of resonances could be valid. The study of the response of the sensor as a function of the viewing angle is important because it states the limits for SiPMs use. Moreover, this function will be of extreme importance for the design of a light concentrator as a focal plane optics.

Further studies should also be performed with respect to the temperature: higher temperature, as stated in chapter 2, increases the phenomena of dark currents and cross-talk, thus a higher spurious count rate is to be expected. It was noted that, during the data acquisition, the temperature in the room varied from 24° to 28°, roughly. A system of refrigerators to ensure a constant temperature is currently under development and investigations in this matter will be done shortly.

As stated in chapter 2 and as can be seen in Figure C.1, SiPMs are much more efficient than PM. In fact, they provide about 57% more detected photons. If we weight their respective efficiency with the Cherenkov flux, we can see that the ratio of the efficiency of the two types of sensors weighted with the Cherenkov spectrum is 1.57. This means that using SiPMs instead of PMs in a telescope camera, the telescope would virtually increase the mirror surface, giving an effective area 1.57 times larger (e.g. LST effective diameter would be 29 m instead of 23 m).

Future developments will surely see SiPMs applied in cameras of LST and other telescopes, since many advantages, with respect to PMs, have been continuously demonstrated and proven.

In CTA, most of the small telescopes are planning to adopt them instead of classical PMs. In the case of LST, from a direct comparison it seems that the increase of efficiency of 1.57% can well capitalize the large cost of the structure. After the construction of the full cluster with SiPM

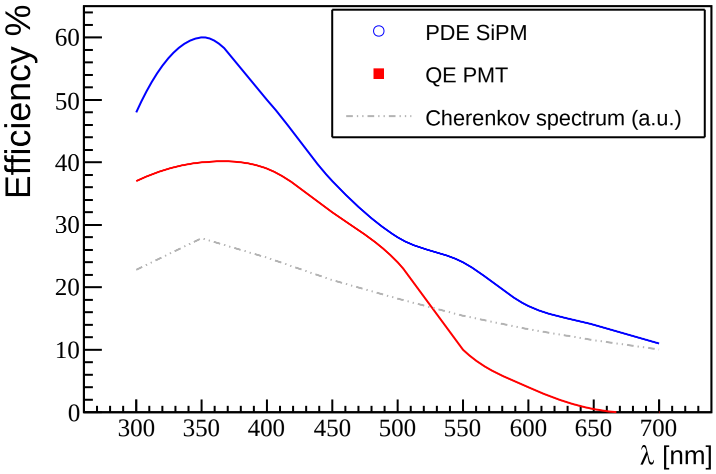

Figure C.1: Detection efficiency of HD3_2 SiPM and a classical phototube

pixels and a comparison of costs and benefits, the collaboration will decide wheter to install the SiPMs in the southern LST telescopes.

Acknowledgments

This work you are now holding would not have been possible without the continuous help and support of several people.

First of all, I would like to thank my relator, Prof. Mosè Mariotti. Without his guide, I would have never completed this thesis. A huge thanks also goes to my co-relator, Dr. Manuela Mallamaci, who was always helpful and kept stimulating me. I would not be here today if it were not for them.

I also want to thank all the people in the astroparticle research group who, directly or indirectly, helped and supported me during these months.

A big thank you goes of course to my family, for keeping up with my mood swings while I was working on this project, for always encouraging me to do my best and for being there when I needed it the most.

To my long-standing friends, thank you for staying with me no matter what; to my new friends and colleagues, thank you for sharing with me these years of study and personal growth.

To my dogs, just thank you. You are such cuties and I love you so much.

Bibliography

[1] A. Biland, et al. JINST 9 (2014) P10012

[2] A. Bouvier, et al. Proc SPIE 8852 (2013) *Photosensor Characterization for the Cherenkov Telescope Array: Silicon Photomultiplier versus Multi-Anode Photomultiplier Tube*

[3] A. M. Hillas, Astroparticle Physics 43 (2013) *Evolution of ground-based gamma-ray astronomy from the early days to the Cherenkov Telescope Arrays*

[4] F. Krennrich, New Journal of Physics 11 (2009) *Gamma ray astronomy with atmospheric Cherenkov telescopes: the future*

[5] E. Lorenz, R. Wagner, R. EPJ H (2012) *Very-high energy gamma-ray astronomy A 23-year success story in high-energy astroparticle physics*

[6] G. Lutz, Springer, 2007 *Semiconductor Radiation Detectors*

[7] M. Mallamaci, M. Mariotti (2018) *Internal Report*

[8] M. Mallamaci, et al. https://doi.org/10.1016/j.nima.2018.09.141 (2018) *Design of a SiPM-based cluster for the Large Size Telescope camera of the Cherenkov Telescope Array*

[9] T. Montaruli PoS ICRC2015 1043 (2016)

[10] Sense Light, 2011 *An Introduction to the Silicon Photomultiplier*

[11] https://www.cta-observatory.org

[12] https://www.hamamatsu.com